# *Strain distribution and load transfer in the polymer-wood particle bond in wood plastic composites*





| | |
|---|---|
| **Citation** | Schwarzkopf, M., & Muszynski, L. (2015). Strain distribution and load transfer in the polymer-wood particle bond in wood plastic composites. Holzforschung, 69(1), 53-60. doi:10.1515/hf-2013-0243 |
| **DOI** | 10.1515/hf-2013-0243 |
| **Publisher** | Walter de Gruyter GmbH |
| **Version** | Version of Record |
| **Terms of Use** | http://cdss.library.oregonstate.edu/sa-termsofuse |

Matthew Schwarzkopf* and Lech Muszynski

# Strain distribution and load transfer in the polymer-wood particle bond in wood plastic composites

**Abstract:** The load transfer between wood particles and the matrix was analyzed by observation of the strain patterns in thin films of high density polyethylene (HDPE) with embedded wood particles subjected to tensile loading. Optical measurement techniques based on the digital image correlation (DIC) principle were employed for quantitative measurement of strain distributions on the surfaces of the specimens. Interpretation of these measurements in terms of load transfer between the particle and the matrix below the surface proved challenging and required a structured approach. In this paper, quantitative descriptors were selected as synthesized metrics to support the quantitative interpretation of the measured strains. X-ray computed tomography (XCT) scans were used to assess the effect of the position of the particles in the film specimens on the strains patterns observed on the surface.

**Keywords:** digital image correlation, load transfer, micromechanics, optical measurement, short fiber composites theory, wood plastic composites

DOI 10.1515/hf-2013-0243
Received December 13, 2013; accepted April 17, 2014; previously published online May 10, 2014

## Introduction

Mechanical performance of wood plastic composites (WPCs) is determined by their morphology, mechanical properties of their individual components, and the internal bonds providing effective load transfer between these components. Bulk mechanical properties of particulate composites like WPCs can be determined by means of standard tests. The development of new and improved composites is a challenge if their properties should be predicted or modeled based on the composition and internal structure of such composites. To-date, the mechanical characteristics of WPCs have been largely studied through testing of bulk materials (Bledzki and Gassan 1999; Stark and Rowlands 2003; Malchev et al. 2005; Bouafif et al. 2009). While testing methods such as tensile, flexural, or impact testing yield useful information on the bulk properties, they can only provide indirect clues on the complex micromechanics of these heterogeneous composites.

In-parallel, analytical approaches and numerical models have been proposed to simulate the micromechanics of particulate and short fiber composites, but their fundamental assumptions were difficult to verify by direct empirical measurements. A comprehensive summary of such methods was compiled by Clyne (1989). One of the first analytical techniques used was the shear lag model based on a paper written by Cox (1952) and has been widely applied to describe the loading of aligned short-fiber composites. Expanding these types of models to a 3D matrix with complex particle interactions and short discontinuous fibers requires some assumptions that cannot be overlooked in case of irregular bio-based particles of wood (Raisanen et al. 1997). Common assumptions of these models are that the embedded particles are impermeable, the particles are cylindrical in shape, a perfect bonding interface exists between the particles, and the matrix and the particles are isotropic.

Clyne (1989) and Noselli et al. (2010) showed a strain field disturbance in the matrix surrounding a rigid embedded particle during tensile loading (Figure 1g and h). Noselli et al. (2010) embedded a steel inclusion in a flexible polymer matrix and observed the photoelastic fringe patterns produced under tension (Figure 1g). Figure 1h was produced by Clyne (1989) and shows a simplified schematic illustration of the strain field disturbance. Both studies tested embedded particles that are dissimilar to those in WPCs and the relationship between the particles and matrices were partly conjectural.

Sretenovic et al. (2006) addressed some of the presumptions often associated with the classic shear lag model. A $2.0\times0.7\times70.0$ mm$^3$ slice of spruce wood was immersed in a molten volume of low density polyethylene-graft-maleic

***Corresponding author: Matthew Schwarzkopf,** Department of Wood Science and Engineering, Oregon State University, 119 Richardson Hall, Corvallis, OR 97331, USA,
e-mail: matthew.schwarzkopf@oregonstate.edu
**Lech Muszynski:** Department of Wood Science and Engineering, Oregon State University, 119 Richardson Hall, Corvallis, OR 97331, USA

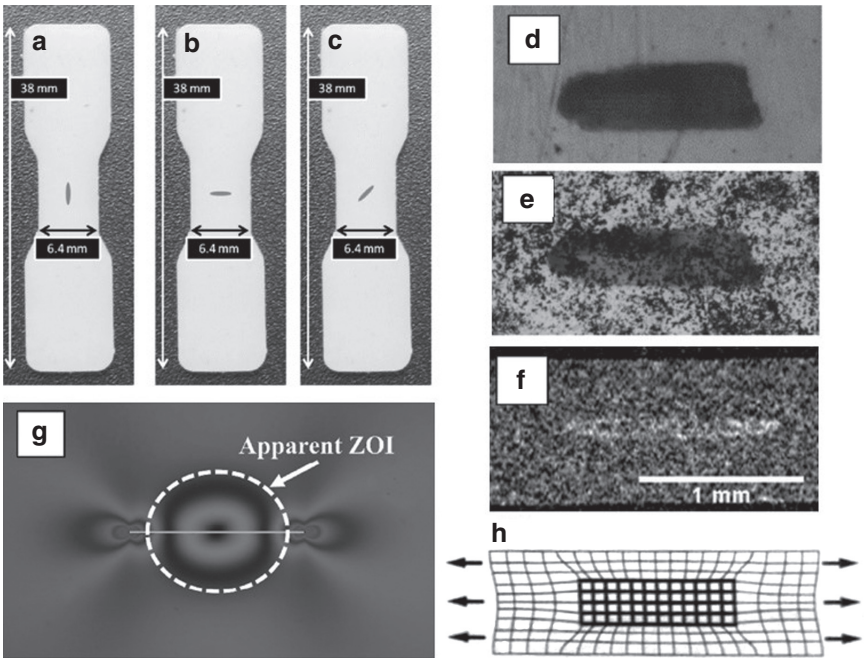


**Figure 1** (a, b, c) WPC test specimens; (d, e) embedded wood particle before and after speckle application; (f) XCT scan of embedded particle; (g) photoelastic fringe patterns of particle in tension (Noselli et al. 2010) (h) schematic illustration of elastic strain around a rigid cylinder (Clyne 1989).

anhydride polymer. From this WPC, 1.2 mm thick slices were cut with the 2.0×0.7 mm$^2$ particle oriented parallel to the axis of loading for subsequent tensile tests. During these tests, optical measurements of the strain distribution patterns surrounding the embedded wood slices were made by means of electronic laser speckle interferometry (ESPI). For validation of the measured strain disturbance patterns, a finite element analysis (FEA) was performed. A general agreement was found between the shear strain distribution patterns around the wood slices measured by ESPI and those predicted theoretically with the classic shear lag model. It was found that there was a significant level of load transfer occurring at the ends of embedded wood slices. This study was successful in developing a methodology to measure strain disturbances around embedded wood slices as well as answering questions about the load transfer capacity occurring at the ends of natural fibers. However, the way that the specimens were manufactured was very different from the process in which bonding between particles and the matrix occurs during the course of industrial compounding, which proceeds extrusion or injection molding.

The methodology in this study aims to build upon the success of Sretenovic et al. (2006) with updated optical measurement techniques, compounded WPC specimens, multiple wood particle orientations, and a quantitative analysis of the optical measurements. The specific objective of this study was to develop an efficient method for the measurement of strain distribution patterns in the matrix material surrounding embedded wood particles that could be useful for quantitative characterization of load transfer between wood particles and polymer matrices in WPCs and for verification of proposed analytical theories and numerical models. The present study is part of a larger project, in which the multimodal experimental characterization is coupled with morphology-based modeling techniques and inverse problem methodology in order to describe correlations between morphology, micromechanics of the internal bonds, and bulk properties of bio-based composites (Sebera and Muszynski 2011).

## Materials and methods

The digital image correlation (DIC) method used to calculate the surface strain patterns in thin films of high-density polyethylene (HDPE) with embedded wood particles was similar to the ESPI method used by Sretenovic et al. (2006). A comprehensive description of both methods and a side-by-side comparison of their efficacy was described by Valla et al. (2011).

Specimen preparation: The polymer Fortiflex HDPE was from Solvay Polymers (Houston, TX, USA). Southern yellow pine (SYP) flour (40-mesh, no. 4020) was obtained from American Wood Fibers (Schofield, WI, USA). Particles from this source have a wide size distribution with the median dimensions 0.77×0.27 mm$^2$ and with a median aspect ratio of about 2.85 (Wang 2007). The particles were dried overnight at 103°C in an approx. 30 mm thick layer in an aluminum tray. Dried particles were compounded with HDPE by means of a counter rotating, twin screw C.W. Brabender® Instruments, Incorporated (South Hackensack, NJ, USA), Intelli Torque Plasti Corder® mixer. HDPE (29.93 g) was added to the mixing chamber preheated to 180°C. The mixing speed was set to 30 rpm. When the torque reached a constant level, a pinch of

wood particles was added to the mixing chamber. This small amount of particles led to a sparse composite, in which individual particles were easily identified and analyzed. The particle-matrix interaction was not affected by neighboring embedded particles.

Once the torque level reached a constant level again, 6 g of the compounded melt material was transferred to a square mold with internal void dimensions of 102×1×02×0.85 $mm^3$ and pre-heated in a small-scale Carver Incorporated (Wabash, IN, USA) Auto M NE, H 3891 hot press to 180°C. The mold assembly with hard stops was held under heat and pressure for 5 min and then transferred to a cold-press until cool to the touch. Test specimens were punched out of the wood-HDPE coupon with a steel dog bone shaped die. The coupon was manipulated in such a way so that a single wood particle was located in the center of the specimen with the orientation at 0°, 45°, and 90° with respect to the loading axis (Figure 1a–c).

In addition to wood particles, idealized specimens with 1 mm sections of tin coated 0.2 mm copper wire embedded in a HDPE matrix served as reference. The wire sections had similar dimensions to the median wood flour particles but were solid (non-porous), isotropic, and had a regular cylindrical geometry, which met some of the assumptions of the short fiber theories previously described. The surface was roughed with 120 grit sandpaper in an attempt to improve the bonding surface. All together nine reference specimens and nine wood specimens were prepared.

Knowledge of the position of the particles in the specimen is important for proper interpretation of the optical measurements and for morphologically accurate modeling. Due to the random nature of the manufacturing process, the wood and wire particles naturally resided throughout the thickness of the specimens. Wang et al. (2007) determined the position of wood particles in their WPC composites by XCT scans. In order to determine the position of the particles within the polymer films for this study, all specimens were scanned in a ScanCo (Brüttisellen, Switzerland) MicroCT XCT scanner at a resolution of 10 µm/voxel (Figures 2 and 3).

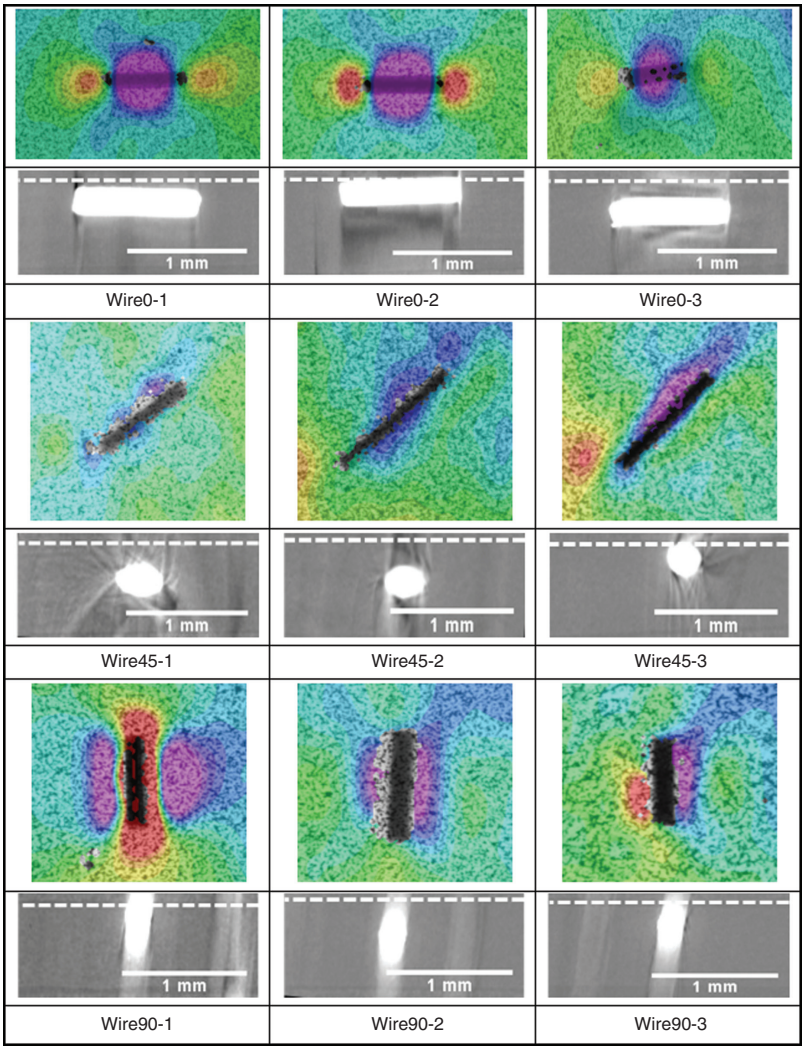


**Figure 2** $\varepsilon_1$ strain plots of reference wire/HDPE composites with corresponding XCT images of particle depth. Specimen surface is marked with a dotted line.
Note: Blurry images and shadows in the XCT data are artifacts from the metal particle affecting the X-ray beam. For color scale ranges, refer to Table 2.

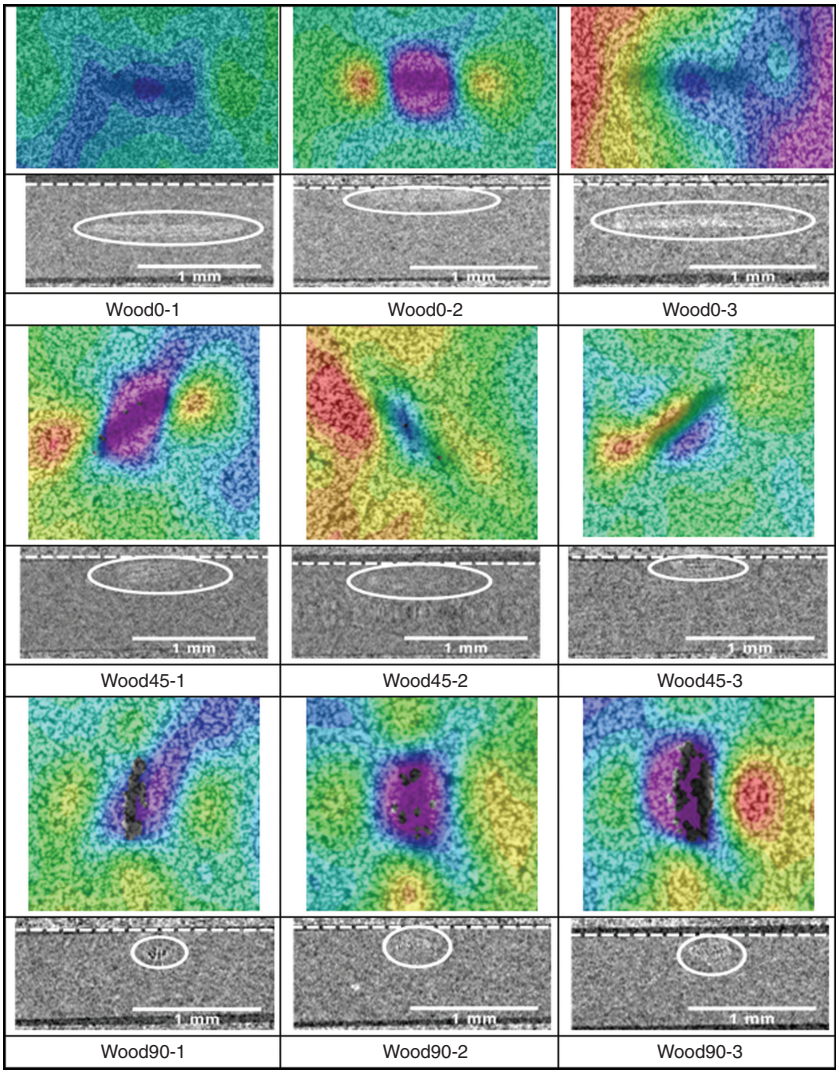


**Figure 3** $\varepsilon_1$ strain plots of wood/HDPE composites with corresponding XCT images of particle depth.
Specimen surface is marked with a dotted line and particles are circled. Note: Wood as a material has a density close to that of HDPE and as such attenuates to a similar degree. This causes the poor material differentiation seen above in the XCT scans. For color scale ranges, refer to Table 2.

Speckle pattern: Toner powder from a Hewlett Packard (Palo Alto, CA, USA) Q2612A cartridge was chosen, which was transferred on specimens by means of custom made air deposition apparatus (M.A. Sutton, personal communication) and was fixed on the surfaces by heating in an oven at 103°C for 10 min.

Tensile test: An Instron (Norwood, MA, USA) ElectroPuls E1000 test machine applied a tensile force at a ramp rate of 0.5 mm $min^{-1}$ (strain equivalent to 0.02 mm $min^{-1}$) for 2 min. The force was measured with a 2527 Series Dynacell (Norwood, MA, USA) load cell (±2 kN capacity). Force and displacement of the cross head was recorded throughout the test with a data acquisition (DAQ) unit.

Optical measurement: Changes in strain distribution patterns in the matrix material surrounding embedded wood particles were measured by an optical measurement system. During the test, images of the specimen surface in the immediate neighborhood of the embedded particles (field of view, 7.18 mm×6.00 mm) were recorded once every second for 2 min with the Correlated Solutions, Incorporated (Columbia, SC, USA) VIC Micro 3D™ system. The basic hardware components for this system consisted of two synchronized cameras and a stereomicroscope. The image sequences were processed with the Correlated Solutions, Incorporated (Columbia, SC, USA) VIC 3D 2010 software.

For each test, an area of interest (AOI) including a single particle and the surrounding area, was selected for analysis manually (Figure 4). The principle parameters of the analysis affecting the accuracy and precision of the analysis were a facet size of 49 pixels and step size of 5 pixels. The output generated by the VIC-3D 2010 software is numerical and can also be presented in the form of color-coded maps plotted and overlaid on the deformed specimen images.

Data analysis: The area of local strain field disturbance in the matrix surrounding the rigid particle marked with a dotted circle in Figure 1g, was considered and referred to as the embedded particle's zone of influence (ZOI) in this study. For a quantitative analysis of the data, a number of descriptors (see Table 1) were developed that refer to the extent, position, and shape of the ZOI around the embedded particle. Particle length and orientation were measured using ImageJ

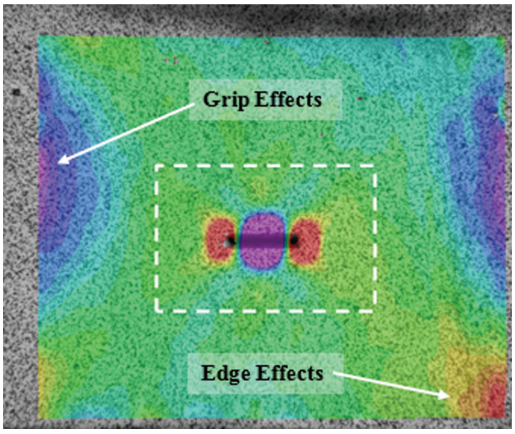


**Figure 4** The effect from the tensile grips (blue/purple) seen on the left and right of the particle and an edge effect in the bottom right. The dotted box shows the area of analysis.

**Table 1** Quantitative descriptors and their derivation.

| Quantitative descriptors | Derivation |
|---|---|
| Particle length (mm) | Measured |
| Particle orientation (degrees from X) | Measured |
| Particle distance from the surface (mm) | Measured |
| Area of ZOI surface section ($mm^2$) | Measured |
| Equivalent radius of ZOI | $r_E = \sqrt{\left(\frac{A_z}{\pi}\right) \cdot d^2}$ |
| Circularity of ZOI ($r^2$) | Calculated |
| Ratio of ZOI equivalent radius to the particle length for 0° and 90° specimens (mm $mm^{-1}$) | $R_{r_E \cdot l} = \frac{r_E}{l}$ |
| Ratio of ZOI minor dimension to the particle depth for 45° specimens (mm $mm^{-1}$) | $R_{Z_m \cdot d} = \frac{Z_m}{d}$ |

$r_E$, equivalent radius; $A_Z$, the area of ZOI surface section; $d$, particle distance from the surface; $l$, particle length; $Z_m$, ZOI's minor dimension.

software (Rasband 1997–2012) based on the test sequence images shown in Figure 1d and e. The distance from the surface was determined from XCT scans (Figure 1f) using ImageJ.

The area of ZOI surface section (Figures 1g and 5c) was measured by counting the DIC data points associated with it. Each point has a physical area associated with it and these areas were added to find the total area. The extent (or size) of the ZOI may be described by an equivalent radius of an idealized spherical ZOI, with the surface section equal to that actually measured (Figure 5c). For specimens at 45°, the ZOI was often elongated along the particle's length and so the equivalent radius was calculated based on the minor dimension of the ZOI, which was measured using x and y coordinates in the direction perpendicular to the major axis of the particle.

The shape of the ZOI may be quantitatively described by its level of circularity. This was measured by simple linear regression of the x and y coordinates of the data points associated with the ZOI. For example, the best fit line of a set of points with a circular distribution would have an $r^2=0$, a set of points in a straight line would have an $r^2=1$, and any intermediate elongated oval distribution would have $0<r^2<1$. The ratio of ZOI equivalent radius to the particle length for 0° and 90° specimens and the ratio of the of ZOI minor dimension to the particle depth for 45° specimens were also calculated.

## Results and discussion

The dimensions (length and width) and positions (angle and depth below the specimen surface) of the embedded particles in the polymer film are summarized in Table 3. During the test, as the matrix was loaded, the load was gradually transferred along the length of the fiber from the fiber end through shear (due to the difference in compliance between the fiber and matrix) so that gradually more of the tensile load was carried by the fiber and less by the surrounding matrix, until the strains in the fiber matched the strain gradient in the matrix. In the low aspect ratio particles measured in these experiments (Wang 2007), the load transfer zones from both ends overlap. In effect, the central part of the fiber never reached the state in which the strains in the fiber were matching the strain gradient in the matrix (Cox 1952; Clyne 1989; Sretenovic et al. 2006; Wang 2007).

The strain distribution related to this load transfer was measured by an optical measurement system. Its accuracy and precision were assessed by analyzing images of unloaded test samples. The expected mean displacements and strains in all directions were zero, and all non-zero values measured were noise generated by the optical measurement system. The mean displacement

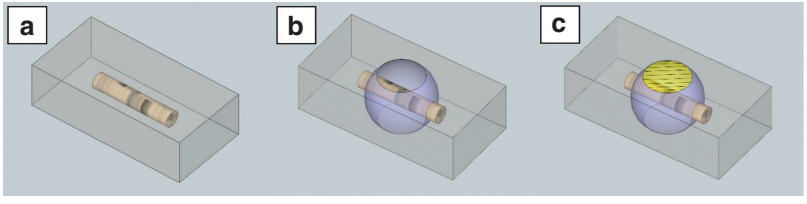


**Figure 5** Idealized schematic of an embedded particle and its influence on the surrounding matrix (a) an idealized wood particle embedded in a polymer matrix (b) partial orbital surrounding the particle representing its ZOI (c) crosshatched circular section signifying the measured section of the ZOI.

and strains from this data provided a measure of accuracy, and their respective standard deviations provided a measure of the system's precision. These two measures depended on many factors, but when all other conditions were equal, the differences reflected the effect of the specific speckle pattern. The speckle pattern materials considered for this study were: 1) lead powder (-200 mesh, 99% metals basis) from Alfa Aesar (Ward Hill, MA, USA) 2) toner powder from a Hewlett Packard (Palo Alto, CA, USA) Q2612A cartridge, and 3) carbon nanopowder (<500 nm, >99.95% trace metals basis) from Sigma-Aldrich (St. Louis, MI, USA). Speckle patterns produced with the toner powder generated the least random noise. The related accuracy and precision of x displacement measurements were ±0.0814 pixels and ±0.0032 pixels respectively. Consequently, toner powder was used in all testing.

The data used for analysis was restricted to a designated rectangular area surrounding the particle in such a way as to crop out the effect of the tensile grips and the edges seen in Figure 4. The areas selected for specimens oriented at 0°, 45°, and 90° were 4×2 mm$^2$, 3×3 mm$^2$, and 2×2 mm$^2$, respectively. These areas were centered with the particle's center coordinates.

Figure 2 shows nine color-coded full-field maps of major principal strain, $\varepsilon_1$, of the reference wire/HDPE specimens. The color scale ranges from red for high strain levels to purple for low strain levels. The specific strain ranges for each orientation group of specimens in Figure 2 are summarized in Table 2. Directly below these maps are their corresponding XCT scans locating their position within the film thickness.

Generally, the extent and the shape of the zone is affected by the bonding efficacy. However, while the actual ZOIs surrounding the embedded particles are three dimensional, the optical measurements were limited to what could be detected on the surface of the specimen, where it intersects with the particle's ZOI (Figure 5c). The deeper the particle was burried below the specimen surface the smaller is the ZOI section detectable on the surface. Comparing the depth of the wire particles below the specimen surface with the area of the ZOI intersection on the surface shows a distinct trend. For instance, Wire0-1 was found 0.020 mm from the surface and had a ZOI intersection area of 0.62 mm$^2$, whereas the depth of Wire0-3 was 0.100 mm and had a ZOI intersection area of 0.41 mm$^2$ (first row in Figure 2). This shape and extent of the zone may have been additionally affected by the particle geometry, length, and orientation. However, for particles of the same shape and orientation the equivalent radius of the three dimensional ZOI was calculated from the dimensions of its intersection on the surface and the average distance of the particle from the surface (particle depth in Table 1).

**Table 2** Minimum and maximum bounds of the color scales for strain ranges for $\varepsilon_1$ strain plots in Figures 2 and 3.

| Specimen groups | $\varepsilon_1$ – min (purple) | $\varepsilon_1$ – max (red) |
|---|---|---|
| Wire0 | 0.0073 | 0.0132 |
| Wire45 | 0.0097 | 0.0147 |
| Wire90 | 0.0094 | 0.0139 |
| Wood0 | 0.0098 | 0.0160 |
| Wood45 | 0.0099 | 0.0138 |
| Wood90 | 0.0115 | 0.0134 |

The strain distribution patterns measured in the 0° orientation specimens (Figure 2) were consistent with the theoretical description of load transfer (Cox 1952; Clyne 1989; Sretenovic et al. 2006). The lower strain regions seen about the center of the particle did suggest that more load was being carried by the embedded particle and the particle was reinforcing the material around it.

In the 0° and 45° specimens, the ZOI, as we have defined it, was associated with the low strain area elongated along the length of the particle. Of interest were the Wire90-1 and Wire90-3 specimens pictured in Figure 2, where there were high strain regions in the ZOI. These areas likely indicated separation of the polymer matrix from the particle. In the absence of a bond between the polymer and the matrix, the embedded particle would act as a filler rather than a reinforcement and would not contribute to increased composite stiffness.

Figure 3 shows nine color-coded full-field maps of major principal strain, $\varepsilon_1$, of the wood/HDPE specimens. The specific strain ranges for each orientation group of specimens in Figure 3 are summarized in Table 2. Directly below these maps are their corresponding XCT scans locating their position within the film thickness.

The strain distribution patterns measured in the 0° orientation specimens were more variable than those seen in the refence specimens (with embedded wire sections). Wood0-2 appeared to be consistent with the patterns seen in the reference specimens, whereas the patterns seen in Wood0-1 and Wood0-3 were less pronounced due to an increased particle distance from the surface. Looking at Table 3, both Wood0-1 and Wood0-3 were embedded over 0.3 mm below the surface of the specimen, supporting that depicted in Figure 5c. At this depth below the surface, measurement of the ZOI intersection area may not be possible.

Of interest were the wood/HDPE specimens at a 90° orientation. Commonly, wood particles are added to the

**Table 3** Measured and calculated descriptor values from Table 1.

| Specimen | PL (mm) | PO (degrees) | PD (mm) | ZOI (mm²) | ER (mm) | C (r²) | ER/L | MD (mm) | MD/D |
|---|---|---|---|---|---|---|---|---|---|
| Wire0-1 | 1.162 | 1.3 | 0.020 | 0.620 | 0.44 | 0.0001 | 0.38 | – | – |
| Wire0-2 | 1.078 | 0.1 | 0.004 | 0.571 | 0.43 | 0.0031 | 0.40 | – | – |
| Wire0-3 | 1.271 | 4.1 | 0.100 | 0.411 | 0.38 | 0.0035 | 0.30 | – | – |
| Wire45-1 | 1.481 | 37.2 | 0.178 | 0.077 | 0.24 | 0.7460 | – | 0.23 | 0.76 |
| Wire45-2 | 1.854 | 42.5 | 0.190 | 0.385 | 0.41 | 0.7270 | – | 0.62 | 0.31 |
| Wire45-3 | 1.630 | 48.3 | 0.017 | 0.403 | 0.37 | 0.7910 | – | 0.49 | 0.03 |
| Wire90-1 | 1.064 | 90.1 | 0.047 | 0.763 | 0.51 | 0.0023 | 0.48 | – | – |
| Wire90-2 | 1.276 | 87.0 | 0.137 | 0.374 | 0.37 | 0.0000 | 0.29 | – | – |
| Wire90-3 | 0.963 | 87.8 | 0.050 | 0.196 | 0.26 | 0.0165 | 0.27 | – | – |
| Wood0-1 | 1.269 | 5.7 | 0.393 | 0.095 | 0.43 | 0.0055 | 0.34 | – | – |
| Wood0-2 | 0.827 | 3.6 | 0.034 | 0.460 | 0.38 | 0.0172 | 0.46 | – | – |
| Wood0-3 | 1.556 | 0.4 | 0.310 | 0.063 | 0.34 | 0.0171 | 0.22 | – | – |
| Wood45-1 | 1.081 | 37.4 | 0.030 | 0.776 | 0.70 | 0.4607 | – | 0.57 | 0.05 |
| Wood45-2 | 1.353 | 39.0 | 0.125 | 0.004 | 0.13 | 0.5270 | – | 0.18 | 0.68 |
| Wood45-3 | 0.969 | 40.7 | 0.010 | 0.098 | 0.18 | 0.4800 | – | 0.22 | 0.05 |
| Wood90-1 | 0.643 | 80.5 | 0.150 | 0.158 | 0.27 | 0.4273 | 0.42 | – | – |
| Wood90-2 | 0.924 | 91.9 | 0.105 | 0.248 | 0.30 | 0.0015 | 0.32 | – | – |
| Wood90-3 | 0.948 | 90.4 | 0.068 | 0.299 | 0.32 | 0.0048 | 0.33 | – | – |

PL, particle length; PO, particle orientation; PD, particle distance from surface; ZOI, ZOI surface area; ER, equivalent radius; C, circularity of ZOI; ER/L, equivalent radius/length; MD, minor dimension; MD/D, minor dimension/depth.

polymer matrix of WPCs as filler. We have seen that these particles have load transfer capacity if aligned with the axis of loading, but these fillers are not typically expected to provide meaningful load transfer if oriented perpendicularly to the axis of loading. The ZOI of specimens Wood90-1 and Wood90-2 indicated a reinforcing effect in the material, whereas Wood90-3 appeared to have delaminated on the right side. It is likely that the polymer matrix and wood particles were to some degree mechanically interlocked due to the porosity of the wood particles.

Measured particle lengths, orientation angle towards the loading direction, distance from the surface, and the ZOI surface intersection area for all specimens were summarized in the first four columns of Table 3. The next four columns summarized the calculated ZOI descriptors that can be used for quantitative comparison of the strain disturbances generated by the embedded particles: the equivalent radius of ZOI, circularity of ZOI surface intersection area, the ratios of ZOI equivalent radius to the particle length (for 0° and 90° specimens), and of ZOI minor equivalent dimension (for 45° specimens) to the particle depth. The ratios may be used to compare ZOIs generated by particles of different sizes.

The graph in Figure 6 shows the relationsip between ZOI area and the particle distance from the surface for all specimens. It can be seen how the area of the ZOI section detectable on the surface increases as a function of decreasing particle depth. This correlaion, however, did not hold for specimens with 45° (Figure 7).

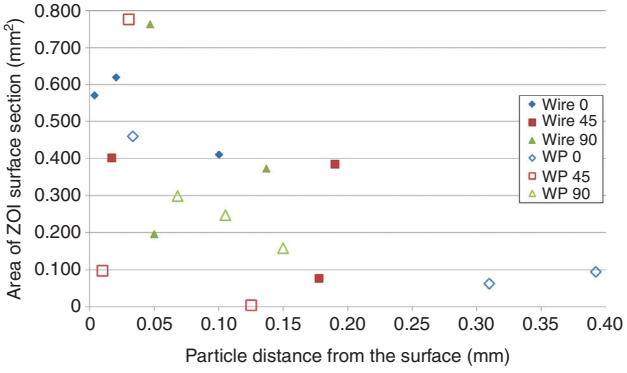


**Figure 6** ZOI area and particle depth relationship for all specimens.

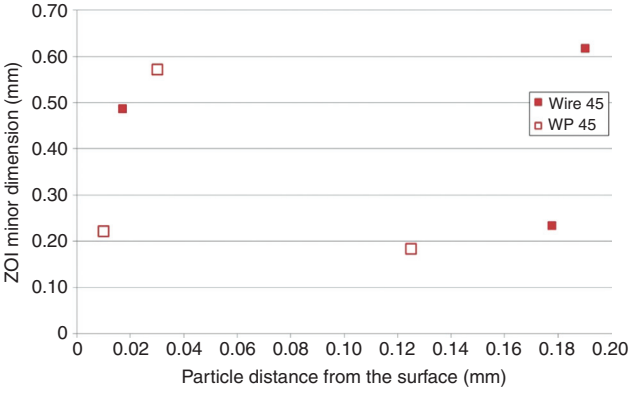


**Figure 7** Relationship between ZOI Minor dimension (45° specimens) and the particle distance from the surface.

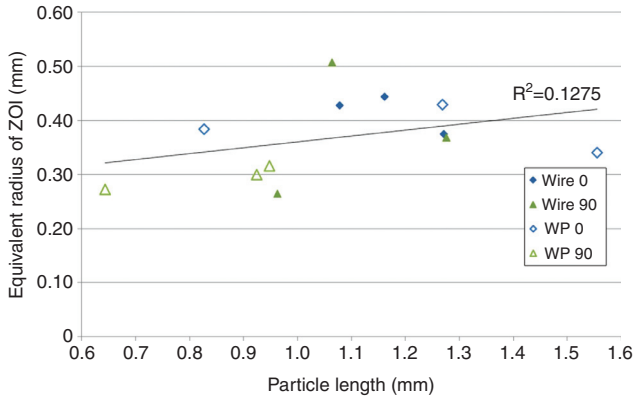


**Figure 8** Equivalent radius and particle length relationship.

There was little correlation between the ZOI equivalent radiuses oriented at 0° and 90° to the loading direction and the particle length (Figure 8). This poor correlation may have been due to this relationship being affected by multiple parameters including particle orientation, and the particle to matrix bonding (the distance from the surface was taken into account in the formula used to calculate the equivalent radius).

As with Sretenovic et al. (2006), this study found agreement between the measured strain distribution patterns (Figures 2 and 3) and the previously modeled results (Figure 1g and h). The high strain regions found at the ends of the fibers indicates that there was a connection with the polymer. If the ends of the particles were disconnected, there would be little axial strain occurring here. For fibers with low aspect ratios like the particles in WPCs, this load transfer area at the ends along with the sides of the fiber was an important component.

This analysis showed that the quantitative analysis of the ZOI alone could hardly be used for assessment of the efficacy of load transfer between polymer matrices and embedded particles. It was expected that better results might be obtained by employing morphologically accurate numerical models of the analyzed specimens. This approach will be reported in a separate publication.

## Conclusions

The overall goal of this research was to develop an efficient method for the measurement of strain distribution patterns in the matrix material surrounding embedded wood particles. Building on the work of Sretenovic et al. (2006), this paper has presented a measurement methodology based on updated optical measurement techniques, compounded WPC specimens, multiple wood particle orientations, and a quantitative analysis of the optical measurements.

It was found that the patterns observed on the surface of the specimen were substantially affected by the particle distance from the surface. This distance is a critical parameter for any comparison of strain patterns. Due to this significant effect, analysis of the load transfer behavior in the polymer-wood particle bond would be best conducted in conjunction with predictive modeling tools.

## References

Bledzki, A.K., Gassan, J. (1999) Composites reinforced with cellulose based fibres. Prog. Polym. Sci. 24:221–274.

Bouafif, H., Koubaa, A., Perré, P., Cloutier, A. (2009) Effects of fiber characteristics on the physical and mechanical properties of wood plastic composites. Composites Part A 40:1975–1981.

Clyne, T.W. (1989) A simple development of the shear lag theory appropriate for composites with a relatively small modulus mismatch. Mater. Sci. Eng. A122:183–192.

Cox, H.L. (1952) The elasticity and strength of paper and other fibrous materials. Br. J. Appl. Phys. 3:72–79.

Malchev, P.G., David, C.T., Picken, S.J., Gotsis, A.D. (2005) Mechanical properties of short fiber reinforced thermoplastic blends. Polymer 46:3895–3905.

Noselli, G., Dal Corso, F., Bigoni, D. (2010) The stress intensity near a stiffener disclosed by photoelasticity. Int. J. Fracture 166:91–103.

Raisanen, V.I., Alava, M.J., Niskanen, K.J., Nieminen, R.M. (1997) Does the shear-lag model apply to random fiber networks? J. Mater. Res. 12:2725–2732.

Rasband, W.S. ImageJ. U.S. National Institutes of Health. Bethesda, MD, USA, 1997–2012.

Sebera, V., Muszynski, L. (2011) Determination of local material properties of OSB sample by coupling advanced imaging techniques and morphology-based FEM simulation. Holzforschung 65:811–818.

Sretenovic, A., Müller, U., Gindl, W. (2006) Mechanism of stress transfer in a single wood fibre-LDPE composite by means of electronic laser speckle interferometry. Composites Part A 37:1406–1412.

Stark, N.M., Rowlands, R.E. (2003) Effects of wood fiber characteristics on mechanical properties of wood/polypropylene composites. Wood Fiber Sci. 35:167–174.

Valla, A., Konnerth, J., Keunecke, D., Niemz, P., Müller, U., Gindl, W. (2011) Comparison of two optical methods for contactless, full field and highly sensitive in-plane deformation measurements using the example of plywood. Wood Sci. Technol. 45:755–765.

Wang, Y. Morphological characterization of wood plastic composite (WPC) with advanced imaging tools: developing methodologies for reliable phase and internal damage characterization. M.S., Oregon State University, 2007.

Wang, Y., Muszynski, L., Simonsen, J. 2007. Gold as an X-ray CT scanning contrast agent: effect on the mechanical properties of wood plastic composites. Holzforschung 61:723.